JOURNAL OF GEOPHYSICAL RESEARCH, VOL. 113, B04408, doi:10.1029/2007JB005155, 2008

Controls on plume heat flux and plume excess temperature

Wei Leng[1] and Shijie Zhong[1]

Received 3 May 2007; revised 16 October 2007; accepted 15 January 2008; published 11 April 2008.

[1] Plume heat flux and plume excess temperature in the upper mantle inferred from surface observations may pose important constraints on the heat flux from the core and mantle internal heating rate. This study examined the relationship between plume heat flux Q_p, core-mantle boundary (CMB) heat flux Q_{cmb} and plume excess temperature ΔT_{plume} in thermal convection using both numerical modeling and theoretical analysis. 3-D regional spherical models of mantle convection were computed with high resolution and for different Rayleigh number, internal heat generation rate, viscosity structures and dissipation number. An analytic model was developed for variations in Q_p and ΔT_{plume} with depth. The results can be summarized as following. (1) Mantle plumes immediately above the CMB carry nearly 80%–90% of the CMB heat flux. (2) Q_p and ΔT_{plume} decrease by approximately a factor of two for plumes to ascend from near the CMB to the upper mantle depth. (3) Our analytic model indicates that the decrease in Q_p and ΔT_{plume} is mainly controlled by the steeper adiabatic gradient of plumes compared with the ambient mantle and the reduction ratios for Q_p and ΔT_{plume} due to this effect depend upon the dissipation number and the distance over which plumes ascend. (4) The subadiabatic temperature also contributes to the reduction of Q_p and ΔT_{plume}, but its contribution is only 20% to 30%. Subadiabatic temperature from our models with >50% internal heating rate ranges from 35 K to 170 K for CMB temperature of 3400°C. (5) Our results confirms that ~70% internal heating rate for the mantle or Q_{cmb} of ~11 TW is required to reproduce the plume-related observations.

Citation: Leng, W., and S. Zhong (2008), Controls on plume heat flux and plume excess temperature, *J. Geophys. Res.*, *113*, B04408, doi:10.1029/2007JB005155.

1. Introduction

[2] Understanding the heat budget of the Earth's mantle is important for studies of dynamic evolution and chemical composition of the Earth's core and mantle. It is generally agreed that the total surface heat flux of the Earth is about 43 TW. Excluding radiogenic heating of ~7 TW in continental crust leads to 36 TW heat flux that can be attributed to mantle convection processes. Three main heating sources for this 36 TW heat flux include the heat flux from the core, Q_{cmb}, the radiogenic heating in the mantle, Q_{rad}, and the heat associated with secular cooling of the mantle, Q_{sec}. However, how these three heating sources are partitioned to make up the total surface heat flux remains unresolved [*Davies*, 1999; *Zhong*, 2006].

[3] Q_{cmb} provides the basal heating for the mantle and controls the cooling of the core, while Q_{rad} and Q_{sec} constitute the internal heating for mantle convection. Mantle upwelling plumes, which may form at the core-mantle boundary (CMB) due to thermal boundary layer instability and rise to the surface to generate hot spot volcanisms [*Morgan*, 1971], have been considered as the most important agent to transfer Q_{cmb} to the Earth's surface. The plume heat flux estimated from swell topography and plate motion is 2.4–3.5 TW [*Sleep*, 1990; *Davies*, 1988]. This is often taken as Q_{cmb}, based on two assumptions: (1) Q_{cmb} is entirely transferred by the plumes and (2) the plume heat flux does not change when plumes rise from the CMB to surface.

[4] However, these two assumptions have been questioned recently based on numerical modeling of mantle convection [*Labrosse*, 2002; *Bunge*, 2005; *Mittelstaedt and Tackley*, 2006; *Zhong*, 2006]. First, *Labrosse* [2002] found from 3-D Cartesian isoviscous models with the Boussinesq approximation that the CMB heat flux is controlled by cold downwellings rather than plumes, and he suggested that the plume heat flux is only a fraction of Q_{cmb}. *Mittelstaedt and Tackley* [2006] quantified the plume heat flux using 2-D numerical models in three different geometries and also found that the plume heat flux in the upper mantle is a fraction of the CMB heat flux. *Bunge* [2005] suggested that subadiabatic temperature may have significant effects on the plume heat flux. On the basis of his 3-D spherical model calculations that may yield as large as 500 K subadiabatic temperature, *Bunge* [2005] suggested that plume heat flux in the upper mantle may only be 1/3 of Q_{cmb}, if plume excess temperature in the upper mantle is ~250 K. However, Bunge did not quantify the plume heat flux as did by *Mittelstaedt and Tackley* [2006].

[1]Department of Physics, University of Colorado at Boulder, Boulder, Colorado, USA.

0148-0227/08/2007JB005155$09.00

Table 1. Physical Parameters

Parameters	Values
Earth radius R_e	6370.0 km
Mantle thickness d	2870.0 km
Surface thermal expansivity[a]	$(2.4–4) \times 10^{-5}$/K
Surface thermal diffusivity[a]	10^{-6} m^2/s
Surface density ρ_0	3300 kg/m^3
Specific heat C_p	1000 J/(kg · K)
Gravitational acceleration g	9.8 m/s^2
Surface temperature T_s	273 K
Olivine-spinel phase change	
Clayperon slope γ_1	3 MPa/K
Density change $\Delta\rho_1/\rho_0$	7.8%
Spinel-Pervoskite phase change	
Clayperon slope γ_2	-3 MPa/K
Density change $\Delta\rho_2/\rho_0$	7.8%

[a]Thermal expansivity decreases by a factor of 5 from the surface to the CMB, while thermal conductivity increases by a factor of 2.18 from the surface to the CMB.

[5] *Zhong* [2006] quantified the depth-dependence of plume heat flux in 3-D regional spherical models of mantle convection with the extended-Boussinesq approximation. *Zhong* [2006] found that the plume heat flux represents a large fraction of Q_{cmb} as plumes form near the CMB, but the plume heat flux decreases continuously by as much as a factor of 2-3 as plumes rise from the CMB to the upper mantle. *Zhong* [2006] suggested that the reduction in plume heat flux as plumes rise is caused by adiabatic cooling and diffusive cooling of plumes and subadiabaticity. *Zhong* [2006] also showed that Q_{cmb} may be required to account for 35% of the surface heat flux from mantle convection, (i.e., internal heating rate for the mantle is 65%), to reproduce plume-related observations including the plume heat flux and plume excess temperature in the upper mantle.

[6] It is important to understand to what extent plume heat flux represents Q_{cmb} and what controls the reduction of plume heat flux as plumes rise. In this paper, we formulated a simple analytic model for plume heat flux and plume temperature variations with depth. We performed model calculations similar to those by *Zhong* [2006], but with a larger parameter space and higher resolution. The higher resolution enables us to better quantify the variations of heat flux and temperature with depth. Also, the larger parameter space, particularly larger activation energy, varying lithospheric viscosity and varying dissipation number, ensures the robustness of our results. We quantified the ratio of plume heat flux to Q_{cmb} and also the ratio of plume heat flux reduction as plumes rise.

[7] This paper is organized as follows. We first describe our models and a plume detection scheme. Then, the results for several groups of models are shown and analyzed. After a simple analytic model for the plume heat flux variation is derived and compared with numerical model results, the plume-related observations are used to constrain the internal heating rate of the mantle. Finally, the main conclusions are drawn and discussed.

2. Model Setup and Plume Detection Scheme

2.1. Model Setup

[8] Our models are similar to those by *Zhong* [2006]. Here we only describe the main features of our models, and for detailed descriptions including governing equations readers should refer to *Zhong* [2006]. We use the extended-Boussinesq approximation to describe mantle convection for an incompressible fluid [*Christensen and Yuen*, 1985]. Our models include an exothermic phase change at 410-km depth and an endothermic phase change at 670-km depth. Our models also take into account of the latent heating from the phase changes, adiabatic heating, viscous heating and radiogenic heating.

[9] Our models employ depth-dependent thermodynamics properties. From the surface to CMB, the coefficient of thermal expansion α decreases by a factor of 5, whereas thermal diffusivity κ increases by a factor of 2.18.

[10] Mantle viscosity in our models is both depth- and temperature-dependent. The nondimensional viscosity is defined as [*Zhong*, 2006]:

$$\eta = \left(1 - 0.9\frac{r - r_i}{r_0 - r_i}\right)\eta_r \times \exp\left\{E\left[1 - \frac{T - T_{adi}(r) + T_{adi}(r_{ttbl})}{\Delta T_{s\_a}}\right]\right\}, \quad (1)$$

where r and T are nondimensional radius and temperature, with r varying from $r_i = 0.55$ at the CMB to $r_o = 1.0$ at the surface. Depth-dependent parameter η_r is 1/30 between 100 km and 670 km depths, and 1 in the lower mantle. We define η_r in the lithosphere (i.e., between the surface and 100 km depth) as η_{r_lith}, which is a variable in our models. E is the nondimensional activation energy. $T_{adi}(r)$ is the adiabatic temperature at radius r and is determined by downward integration of adiabatic gradient $g\alpha(r)T_{ave}(r)/C_p$ [*Turcotte and Schubert*, 2002] from the base of the top thermal boundary layer r_{ttbl} where the adiabatic temperature is $T_{adi}(r_{ttbl})$. In the adiabatic gradient, g, $\alpha(r)$, $T_{ave}(r)$ and C_p are gravitational acceleration, coefficient of thermal expansion at radius r, average temperature at radius r, and specific heat, respectively. ΔT_{s_a} is the total super-adiabatic temperature difference from the CMB to surface.

[11] The Rayleigh number is defined using the thickness of the mantle, surface values of coefficients of thermal expansion and thermal diffusivity, and viscosity at the CMB. The equation for definition of Rayleigh number is given by *Zhong* [2006]. We use the thickness of the mantle to define the dissipation number instead of the Earth radius that was used by *Zhong* [2006]:

$$D_i = \frac{\alpha_0 g d}{C_p}, \quad (2)$$

where α_0 and d are the surface value of coefficient of thermal expansion and the thickness of the mantle. The model parameters are shown in Table 1.

[12] The domain of our regional spherical models is from 0.55 to 1 in radial direction for nondimensional radius, 65° to 115° in colatitude direction, and 0° to 55.3° in longitude direction. The three governing equations are solved with a parallel finite element code CitcomCU [*Moresi and Gurnis*, 1996; *Zhong*, 2006]. The typical resolution used for the computation is 256, 192 and 64 elements in longitude, colatitude and radial directions, respectively. The number of elements used here is the same as by *Zhong* [2006]. Since

Table 2. Parameters Setup of Different Models[a]

Case	$Ra(10^7)$	H	E	η_{r_lith}	D_i	*Resol*
WM01	12	72	6.91	1	1.17	Hi
WM02	12	108	6.91	1	1.17	Hi
WM03	12	36	6.91	1	1.17	Hi
WM04	4	36	6.91	1	1.17	Hi
WM04L	4	36	6.91	1	1.17	Lo
WM05	4	72	6.91	1	1.17	Hi
WM06	4	18	6.91	1	1.17	Hi
WM07	1.33	54	6.91	1	1.17	Lo
WM08	1.33	36	6.91	1	1.17	Lo
WM09	1.33	18	6.91	1	1.17	Lo
WM10	4	54	9.21	1/3	1.17	Lo
WM11	4	36	9.21	1/3	1.17	Lo
WM12	4	18	9.21	1/3	1.17	Lo
WM13	4	96	6.91	0.5	1.17	Lo
WM14	4	48	6.91	0.5	1.17	Lo
WM15	4	24	6.91	0.5	1.17	Lo
WM16	4	54	6.91	10	1.17	Lo
WM17	4	36	6.91	10	1.17	Lo
WM18	4	18	6.91	10	1.17	Lo
WM19	4	96	6.91	0.5	0.82	Lo
WM20	4	48	6.91	0.5	0.82	Lo
WM21	4	24	6.91	0.5	0.82	Lo
WM22	4	96	6.91	0.5	0.70	Lo
WM23	4	48	6.91	0.5	0.70	Lo
WM24	4	24	6.91	0.5	0.70	Lo
A01	2.3	23	6.91	1	1.05	Lo
A02	1.8	23	6.91	1	0.84	Lo
A03	1.2	23	6.91	1	0.56	Lo
A03H	1.2	23	6.91	1	0.56	Hi
A04	0.8	23	6.91	1	0.35	Lo
A05	1.5	23	6.91	1	0	Lo
A05H	1.5	23	6.91	1	0	Hi

[a] *Ra*, *H*, *E*, η_{r_lith}, D_i and *Resol* are Rayleigh number, internal heating parameter, activation energy, η_r in lithosphere, dissipation number, and resolution, respectively. In resolution column, Hi and Lo represent 256 × 192 × 64 and 144 × 128 × 64, respectively. Cases WM01 to WM24 include the phase changes and depth-dependent α and κ, while cases A01 to A05 exclude the phase changes and use uniform α and κ. Cases WM04L, A03H and A05H are used for resolution tests.

our box size is only half of dimension in longitude and colatitude directions compared with that used by *Zhong* [2006], our resolution is actually four times higher. This higher resolution helps detect and analyze plumes. Running the code on 24 Pentium 4 Xeon 2.4 GHz processors, it usually takes ~8 days for each model to reach a statistically steady state. We analyze the results over 30,000 time steps after a model reaches a statistically steady state.

2.2. A Plume Detection Scheme

[13] In order to study the dynamics of plumes, we need to quantify the properties of plumes in convection models. First, we quantify temperature profiles of the mantle. $T_{\max}(r)$ and $T_{ave}(r)$ are the maximum temperature and averaged temperature at different radius r, respectively.

[14] We define and locate upwelling plumes using the same scheme as by *Zhong* [2006] which is similar to that by *Labrosse* [2002]. Two parameters, f and r_{arc}, are used to define the plumes. Here, parameter f determines the temperature threshold $T_{thre\_mid}(r)$ for the maximum temperature of a plume:

$$T_{thre\_mid}(r) = T_{ave}(r) + f[T_{\max}(r) - T_{ave}(r)]. \quad (3)$$

At radius r, only when the maximum temperature of an upwelling is higher than $T_{thre\_mid}(r)$, the upwelling is qualified as a plume. Parameter r_{arc} controls the maximum radial extent of a plume. The plume detection can be described as following. For a given radius r, all the elements at this radius are first indicated as unmarked. The detection scheme searches all the unmarked elements, and finds the element with the maximum temperature. If the maximum temperature is higher than T_{thre_mid}, this element is defined as the center of a new plume. All the unmarked elements in the vicinity of the plume center are examined. An element is marked as part of this plume if its temperature is higher than a threshold background temperature T_{thre_edge}, its radial velocity is upward, and its distance to the center is smaller than r_{arc}. After a plume is detected, the detection will start again for the next plume until there is no new plume found at this radius. Then the detection moves to next radius. We use T_{ave} as T_{thre_edge}, but we also examined the effect of T_{thre_edge} on our plume detection scheme, as will be discussed later.

[15] After all the plumes are identified, the total plume heat flux $Q_p(r)$ is computed as:

$$Q_p(r) = \int_S q_{adv} dS, \quad (4)$$

where S is the plume area, $q_{adv} = u_r[T - T_{ave}(r)]$ is the convective heat flux, with u_r as radial velocity. Similarly, we define the plume mass flux $M(r)$ as:

$$M(r) = \int_S u_r dS. \quad (5)$$

[16] To determine the plume temperature at a given radius r, we take the maximum temperature of each plume at this radius, and compute the averaged plume temperature $T_p(r)$ for all the plumes. After $T_p(r)$ is obtained, the plume excess temperature is simply defined as

$$\Delta T_{plume}(r) = T_p(r) - T_{ave}(r). \quad (6)$$

3. Results

3.1. The Plume Heat Flux and Plume Excess Temperature

[17] Twenty nine models with different parameters are computed (Table 2). We first present case WM01 with Rayleigh number $Ra = 1.2 \times 10^8$, internal heat generation $H = 72$, and activation energy $E = 6.91$. This activation energy leads to viscosity variations of 10^3 for temperature varying from the CMB to surface. A representative steady state thermal structure shows well developed upwelling plumes and downwelling slabs (Figure 1). The horizontally averaged temperature $T_{ave}(r)$ decreases with radius due to the adiabatic cooling, but the plume temperature $T_p(r)$ decreases more rapidly than $T_{ave}(r)$ (Figure 2a). The elevated $T_{ave}(r)$ and $T_p(r)$ in the upper mantle are caused by the latent heating of 410-km and 670-km phase changes. Here, plumes are detected using the schemes described in section 2.2 with $f = 0.2$, $r_{arc} = 0.15$ (i.e., 950 km) and $T_{thre\_edge} = T_{ave}(r)$. The effects of these parameters will be discussed later. Temperature, convective heat flux and identified plume regions are shown in Figure 3 for 1970 km and 300 km depths. We also determine the mantle adiabat $T_{adi}(r)$

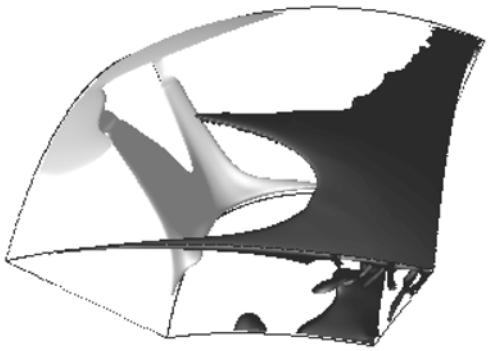

Figure 1. A representative snapshot of residual temperature $T - T_{ave}(r)$ for case WM01 after it reaches a statistically steady state. The light shaded and dark shaded isosurfaces are for residual temperature of 0.09 and −0.09, respectively.

by integrating the adiabatic temperature gradient [*Turcotte and Schubert*, 2002; *Zhong*, 2006] from the upper mantle to CMB, assuming that the adiabatic temperature in the upper mantle (i.e., 300 km depth) is the same as T_{ave} (Figure 2a). The averaged temperature $T_{ave}(r)$ is slightly smaller than $T_{adi}(r)$ for most of the mantle, and the difference between $T_{adi}(r)$ and $T_{ave}(r)$ is subadiabatic temperature.

[18] The depth-dependent plume heat flux and total heat flux normalized by the surface heat flux are presented in Figure 2b. We do not analyze plumes near the top and bottom thermal boundary layers (TBLs) because plumes are not well defined there. As observed by *Zhong* [2006], the plume heat flux decreases as plumes rise from near the CMB to the upper mantle. The phase changes cause significant variations in local heat flux, but they do not change the general trend (Figure 2b). The total heat flux increases continuously from the CMB to surface due to the internal heating. The internal heating rate is defined as $\zeta_m = (Q_s - Q_{cmb})/Q_s$, where Q_s and Q_{cmb} are the heat flux at the surface and the CMB, respectively. The internal heating rate for case WM01 is determined to be 54%. For thermal convection at a perfectly steady state the difference between Q_s and Q_{cmb} should be equal to the internal heating which is the product of the internal heat generation, H and the volume of the model, V. For case WM01, $Q_s = 25.8$, $Q_{cmb} = 11.9$ and $HV = 16.3$. The ∼9% difference between Q_s and $Q_{cmb} + HV$

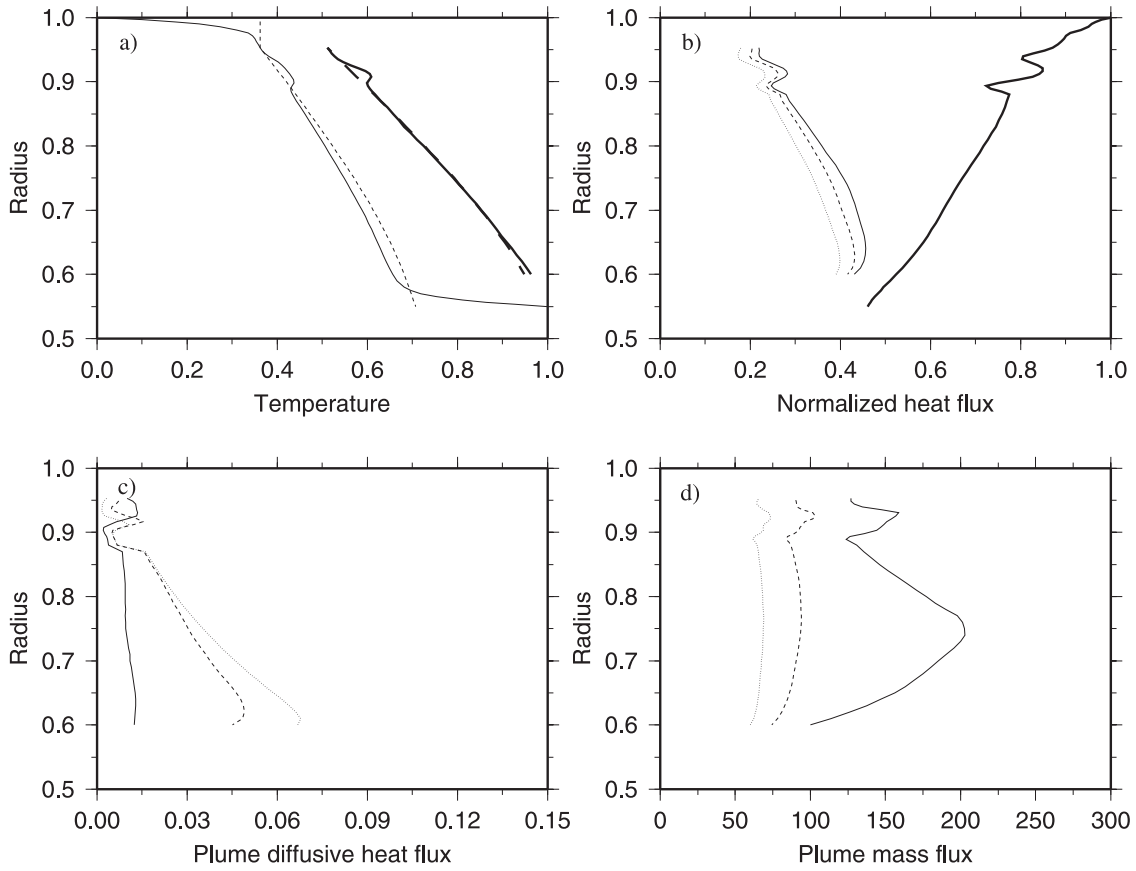

Figure 2. The time averaged results of case WM01 over 30,000 time steps after the convection reaches a statistically steady state. (a) The temperature profiles. The thick and thin solid lines are for the plume temperature $T_p(r)$ and mantle average temperature $T_{ave}(r)$, respectively. The thick and thin dashed lines are the adiabatic temperatures for plumes and the mantle, respectively. (b) The plume heat flux $Q_p(r)$ using different T_{thre_edge} and total heat flux (thick solid line), both normalized by the surface heat flux Q_s. The thin solid, dashed and dotted lines represent the plume heat flux using T_{ave}, $T_{0.1}$ and $T_{0.2}$ as T_{thre_edge}, respectively. (c) The diffusive heat flux $Q_{diff}(r)$ from plume side boundaries and (d) plume mass flux $M(r)$ for T_{thre_edge} equal to T_{ave}, $T_{0.1}$ and $T_{0.2}$, with the same line convention as in Figure 2b.

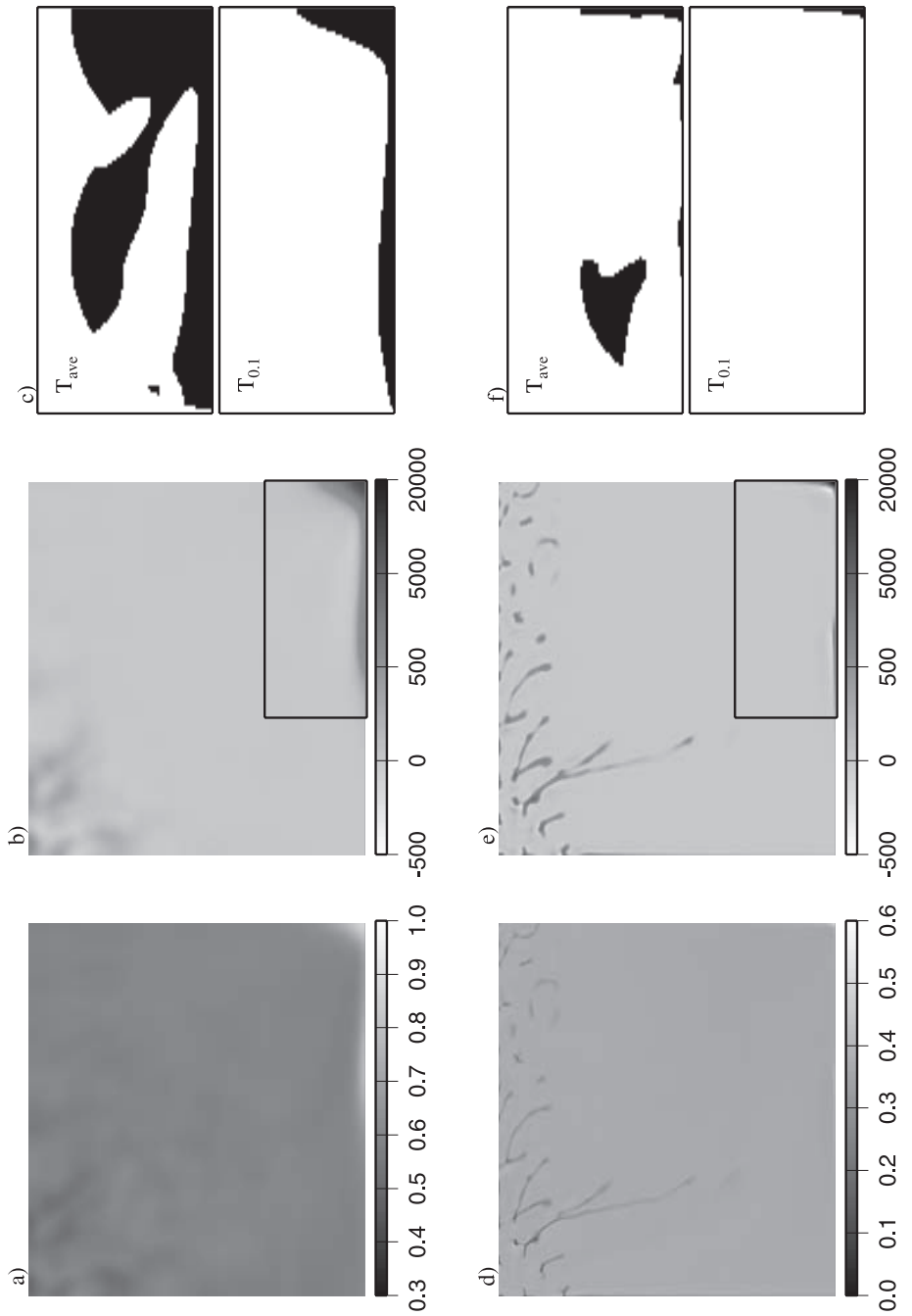

Figure 3. The temperature, convective heat flux, and plume area detected using different T_{thre_edge} for case WM01. Figures 3a and 3d are for temperature at the 1970 km and 300 km depths, respectively. Figures 3b and 3e are convective heat flux and Figures 3c and 3f show identified plume regions at these two depths. Notice that the detected plume regions are constrained in the boxes shown in Figures 3b and 3e, so we exaggerated this region and show them in Figures 3c and 3f. The top panels in Figures 3c and 3f are for $T_{thre\_edge} = T_{ave}$, while the bottom panels are for $T_{thre\_edge} = T_{0.1}$.

indicates that there are still some long-term variations in the bulk temperature of the domain after more than 100,000 time steps of integration. However, such long-term variations do not affect our results on plume dynamics.

[19] As shown by *Zhong* [2006], an important feature of plume heat flux is its reduction as plumes rise. The maximum plume heat flux $Q_{p\_\max}$ occurs at some distance above the bottom TBL or at a radius $r_{\max}$ (Figure 2b). For case WM01, $r_{\max}$ is ~0.64, about 600 km above the CMB. $Q_{p\_\max}$ accounts for 96% of the CMB heat flux Q_{cmb} (Figure 2b). In other words, most Q_{cmb} is carried by plumes immediately above the CMB. However, the plume heat flux accounts for significantly smaller fraction of Q_{cmb} as plumes rise to the upper mantle because of the reduction in plume heat flux. If Q_{p_um} is defined as plume heat flux at r_{um} = 0.953 (or 300 km depth), the ratio of $Q_{p\_\max}$ to Q_{p_um} is found to be ~2.0. This suggests that the plume heat flux is reduced by a factor of ~2.0 as plumes rise from $r_{\max}$ to r_{um}, and that the plume heat flux in the upper mantle is only responsible for ~46% of the CMB heat flux for this case. Plume excess temperature ΔT_{plume} is strongly related to plume heat flux. We also quantify the plume excess temperature in the upper mantle (i.e., 300 km depth), ΔT_{plume_um}, and at $r_{\max}$, $\Delta T_{plume\_\max}$. For case WM01, the ratio of $\Delta T_{plume\_\max}$ to ΔT_{plume_um} is also ~2.0, suggesting that the reduction in plume excess temperature and plume heat flux are related to each other.

[20] To understand the plume heat flux variation with depth, we quantify the total diffusive heat flux Q_{diff_total} from the lateral boundaries of plumes and its contribution to plume heat flux reduction. The following scheme is used to quantify the diffusive heat flux: (1) Mark the elements at the plume boundaries for a give depth or radius r. (2) Determine the temperature gradients in longitude and colatitude directions for each plume boundary element. (3) Determine the diffusive heat flux for each plume boundary element by multiplying the temperature gradient with the corresponding lateral area and diffusivity κ. (4) Sum the diffusive heat flux for each plume boundary element to obtain the diffusive heat flux $Q_{diff}(r)$ at the given radius r. A noticeable trend in $Q_{diff}(r)$ is its moderate increase with depth in the lower mantle (Figure 2c), possibly due to the the effects of increased plume area and thermal diffusivity with depth. Integrating $Q_{diff}(r)$ at different depth leads to diffusive heat flux from plumes Q_{diff_total}. For case WM01, Q_{diff_total} is approximately 0.4, which is less than 4% of the plume heat flux at $r_{\max}$ of 11.8, indicating that the diffusive cooling has a negligible effect on plume heat flux reduction as plumes rise.

[21] In identifying plumes and computing plume heat flux for this case, parameters f = 0.2 and r_{arc} = 0.15 are used. We find that varying f between 0.1 and 0.3, or varying r_{arc} between 0.1 (637 km) and 0.2 (1274 km), has negligibly small effects on plume results (less than 1%). In our study, we use T_{ave} as the threshold temperature T_{thre_edge} to detect the areal extent of plumes. We also examine the effects of T_{thre_edge} on our results by increasing T_{thre_edge} from $T_{ave}(r)$ to $T_{0.1} = T_{ave}(r) + 0.1[T_{\max}(r)\text{-}T_{ave}(r)]$ and $T_{0.2} = T_{ave}(r) + 0.2[T_{\max}(r)\text{-}T_{ave}(r)]$. As expected, the identified area of plumes decreases when T_{thre_edge} increases. The bottom panels of Figures 3c and 3f show the identified plume regions at 1970 km and 300 km depths for $T_{thre\_edge} = T_{0.1}$. Notice that in Figure 3f with $T_{thre\_edge} = T_{0.1}$, there are ~50 elements in the plume region. The decreased plume area for increased T_{thre_edge} causes plume heat flux and plume mass flux to decrease (Figures 2b and 2d). However, the reduction in plume heat flux is uniform at different depth and is generally small compared with the total plume heat flux, suggesting that our plume heat flux result is stable for different T_{thre_edge}. It should be noticed that the plume mass flux is relatively constant as plumes rise from near the CMB to surface for a given T_{thre_edge} (Figure 2d), indicating that there is little material exchange between plumes and the ambient mantle. Increased T_{thre_edge} also leads to increased diffusive heat flux (Figure 2c). The diffusive heat flux Q_{diff_total} is 8% and 9% of $Q_{p\_\max}$, for $T_{thre\_edge} = T_{0.1}$ and $T_{thre\_edge} = T_{0.2}$, respectively, which is still one magnitude smaller than $Q_{p\_\max}$.

[22] The viscous heating and adiabatic heating tend to concentrate in the thermal boundary layers including upwellings and downwellings [*Bercovici et al.*, 1992; *Zhang and Yuen*, 1996]. Figures 4a and 4b show the adiabatic heating and viscous heating at 1970 km depth, and the results are consistent with previous studies [*Bercovici et al.*, 1992; *Zhang and Yuen*, 1996]. We wish to point out that at the mid-mantle depth, the viscous heating is significantly smaller in magnitude than the adiabatic heating (Figures 4a and 4b), although the opposite is expected in the top and bottom thermal boundary layers where horizontal motion is dominant. Particularly important for this study is that the magnitude of adiabatic heating for upwelling plumes is significantly larger than that for downwellings (Figure 4a). This can be understood in terms of the energy balance. The total adiabatic heating must be in balance with total viscous heating for steady state convection [*Turcotte et al.*, 1974; *Hewitt et al.*, 1975; *Jarvis and Mckenzie*, 1980] and also at any time for time-dependent convection [Leng, W., and S. Zhong, Viscous heating and adiabatic heating in compressible mantle convection, submitted to *Geophys. J. Int.*, 2007]. While viscous heating is positive everywhere, adiabatic heating is positive in downwelling regions but negative (i.e., cooling) for upwelling plumes (Figures 4a and 4b). Therefore the magnitude of adiabatic heating term for upwelling plumes must be significantly larger than that for downwellings. This effect is important for causing reduction in plume excess temperature and plume heat flux as plumes ascend. We also show horizontal velocity at 2770 km depth near the CMB in Figure 4c, which shows that the generation of plumes is strongly affected by the downwellings, as *Sleep* [1992] suggested.

[23] Characteristic flow velocities including averaged surface velocity and vertical velocities for the mantle and plumes are useful in understanding the general flow pattern. For case WM01, the averaged surface velocity and vertical velocities for the mantle and plumes in dimensionless form are about 5000, 2000, and 7000, respectively, or about 2.5, 1.0, and 3.5 cm/a, respectively if they are scaled to dimensional form [*Zhong*, 2006]. Considering the horizontal and vertical dimensions of our models, the age of lithosphere at subduction, vertical transit time, and the rising time for plumes are about 255, 82 and 287 Ma, respectively. It should be pointed out that Rayleigh number Ra or convective vigor in our models is still too small compared to that for the Earth's mantle. However, as

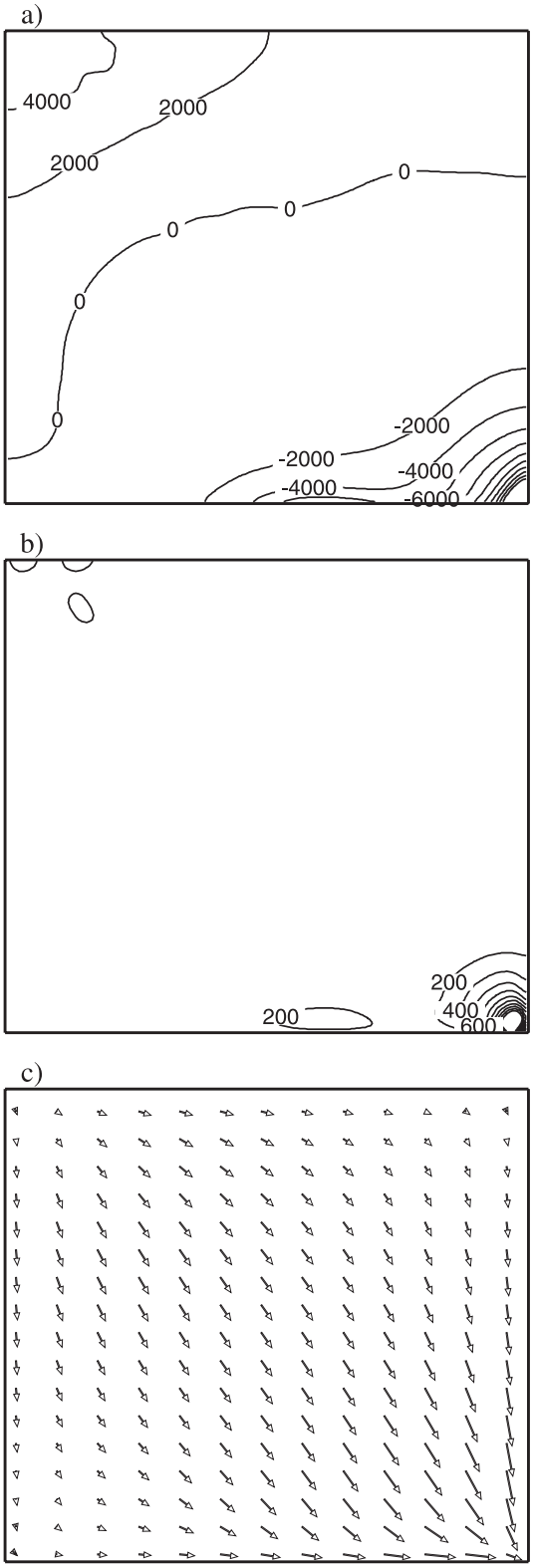

Figure 4. The distribution of adiabatic heating (a), viscous heating (b) at the 1970 km depth and horizontal velocity at the 2770 km depth (c) for case WM01. The interval of the contours in Figures 4a and 4b are 2000 and 200, respectively.

demonstrated by *Zhong* [2006] and later in this study, our main conclusions are insensitive to *Ra*.

[24] We now present cases with different Rayleigh number *Ra*, internal heat generation *H*, activation energy *E* and dissipation number D_i. Cases WM02 to WM09 differ from case WM01 in having different *Ra* and *H* (Table 2). In these cases, *Ra* varies between 1.2×10^8 and 1.33×10^7, and H changes between 18 and 108. As described by *Zhong* [2006], for a fixed *Ra*, increasing *H* tends to increase averaged mantle temperature $T_{ave}(r)$ and surface heat flux Q_s, but to decrease plume heat flux $Q_p(r)$ and CMB heat flux Q_{cmb}. For a fixed H, increasing *Ra* causes all the heat flux to increase, but averaged mantle temperature $T_{ave}(r)$ to decrease. This is confirmed by results for cases WM01 to WM09 (Table 3). Additionally, cases WM02 to WM09 show similar depth-dependence for plume heat flux $Q_p(r)$ and plume temperature $T_p(r)$ to case WM01.

[25] Our resolution test demonstrates that for $Ra = 4.0 \times 10^7$ or smaller, grid with $144 \times 128 \times 64$ elements is sufficient (Table 3 for cases WM04 and WM04L). Therefore this resolution is used for cases WM07 to WM24, but $256 \times 192 \times 64$ resolution is used for cases WM01 to WM06 (Table 2).

[26] Rheological properties and dissipation number are varied in cases WM10 to WM24, in which *Ra* is fixed at 4.0×10^7. Cases WM10 to WM12 use larger activation energy $E = 9.21$ but different *H*. $E = 9.21$ renders the viscosity contrast of 10^4 for temperature varying from 0.0 to 1.0. To maintain significant surface motion and subduction, the pre-exponential factor in the rheological equation (i.e., equation (1)) for the top 100 km, η_{r_lith}, is reduced from 1 for preceding cases to 1/3 to offset the effects of increased *E* on lithospheric viscosity. The higher activation energy may increase the viscosity contrast between the plumes and the ambient mantle. For case WM01 with $E = 6.91$, the viscosity contrast between the plumes and the ambient mantle is about 15, while it is about 30 for case WM11 with $E = 9.21$. Cases WM13 to WM15 use $E = 6.91$, a reduced $\eta_{r\_lith} = 0.5$ and different *H* (Table 2). For all these cases (WM01 to WM15), there is significant subduction and the surface motion is comparable with that in the upper mantle. The ratios of the upper mantle velocity to the surface velocity, R_v, are all about 2 (Table 3). Cases WM16 to WM18 have a higher viscosity in lithosphere with $\eta_{r\_lith} = 10$ and $E = 6.91$. For these three cases, lithospheric motion is much smaller than that in the upper mantle with $R_v > 10$ (Table 3), and there is very little subduction, similar to that in stagnant-lid convection. Dissipation number D_i is an important parameter which affects the viscous heating and adiabatic heating terms. Cases WM01 to WM18 use the same dissipation number $D_i = 1.17$. We change dissipation number to $D_i = 0.82$ and $D_i = 0.70$ for cases WM19-WM21 and WM22-WM24, respectively, but keep $\eta_{r\_lith} = 0.5$ and $E = 6.91$ (Table 2).

[27] For all these cases, the ratios of maximum plume heat flux immediately above the CMB at $r_{\max}$, $Q_{p\_\max}$, to CMB heat flux, Q_{cmb}, are nearly 0.9 (Figure 5a). This result is insensitive to model parameters and shows that the plume heat flux immediately above the CMB accounts for most of the CMB heat flux. Notice that for some cases, especially cases WM16 to WM18 with small surface motion, the ratio of $Q_{p\_\max}$ to Q_{cmb} could be even greater than 1.0. This is because $r_{\max}$ for these cases are relatively large at about 0.7

Table 3. Results[a]

Case	ζ(%)	Q_s	Q_{cmb}	$r_{\max}$	Q_{p_um}	$Q_{p\_\max}$	ΔT_{plume_um}	$\Delta T_{plume\_\max}$	R_v
WM01	54	25.8	11.9	0.64	5.6	11.8	0.149	0.292	1.8
WM02	65	28.9	10.1	0.63	4.4	9.7	0.095	0.218	2.4
WM03	37	21.8	13.7	0.63	7.0	12.5	0.226	0.425	1.3
WM04	46	18.6	10.1	0.64	5.2	9.9	0.181	0.356	1.7
WM04L	46	18.7	10.2	0.64	5.3	10.1	0.176	0.355	1.7
WM05	65	22.2	7.8	0.65	4.0	8.0	0.125	0.223	2.7
WM06	35	16.4	10.7	0.65	5.6	9.4	0.236	0.449	1.3
WM07	66	20.5	7.0	0.64	2.5	6.1	0.116	0.259	1.4
WM08	55	15.0	6.7	0.73	3.4	6.8	0.151	0.267	2.4
WM09	37	13.0	8.1	0.67	3.9	7.5	0.200	0.402	1.6
WM10	54	15.1	7.0	0.65	3.4	6.4	0.152	0.305	2.0
WM11	48	14.1	7.4	0.65	3.5	6.4	0.170	0.349	1.8
WM12	29	13.1	9.3	0.67	4.8	8.6	0.235	0.454	1.5
WM13	68	26.2	8.4	0.62	3.2	7.5	0.106	0.233	1.8
WM14	51	20.6	10.1	0.64	5.1	9.1	0.183	0.369	1.2
WM15	35	17.6	11.4	0.66	5.9	10.1	0.222	0.445	1.1
WM16	59	15.6	6.4	0.75	4.2	7.3	0.112	0.186	35.8
WM17	39	12.9	7.9	0.70	4.7	7.9	0.167	0.295	17.1
WM18	32	12.2	8.3	0.70	4.9	8.2	0.183	0.325	14.5
WM19	48	23.6	12.2	0.64	6.4	10.4	0.256	0.464	1.1
WM20	65	29.9	10.4	0.62	3.7	8.5	0.160	0.318	1.6
WM21	33	19.7	13.2	0.66	7.7	11.7	0.330	0.549	1.1
WM22	49	26.5	13.4	0.66	7.1	11.9	0.287	0.467	1.1
WM23	65	32.6	11.5	0.63	4.8	10.0	0.154	0.338	1.5
WM24	35	19.6	12.9	0.64	6.8	11.0	0.335	0.563	1.1

[a] ζ%, Q_s, Q_{cmb}, $r_{\max}$, Q_{p_um}, $Q_{p\_\max}$, ΔT_{plume_um}, $\Delta T_{plume\_\max}$, and R_v are internal heating rate, surface heat flux, CMB heat flux, radius at which plume heat flux is maximum, plume heat flux at r_{um}, plume heat flux at $r_{\max}$, plume excess temperature at r_{um}, plume excess temperature at $r_{\max}$, and ratio of the upper mantle velocity to the surface velocity, respectively.

(Table 3), and the plume heat flux is influenced by the internal heating between the CMB and $r_{\max}$. Increasing T_{thre_edge} from T_{ave} to $T_{0.1}$ or $T_{0.2}$ slightly decreases the ratios of $Q_{p\_\max}$ to Q_{cmb} (Figure 5b for $T_{thre\_edge} = T_{0.2}$). Therefore we conclude that $Q_{p\_\max}$ accounts for most (80%–90%) of Q_{cmb}.

[28] The ratios of $Q_{p\_\max}$ to plume heat flux in the upper mantle, Q_{p_um}, are all nearly 2.0 and increase slightly with internal heating rate (Figure 6a). For plume excess temperature, the ratios of $\Delta T_{plume\_\max}$ to ΔT_{plume_um} show similar features (Figure 6b), suggesting that variations in plume heat flux are related to variations in plume excess temperature. Notice that for cases WM19-WM24 with reduced dissipation number, these ratios are a little smaller compared with other cases with larger dissipation number. The results for increasing T_{thre_edge} from T_{ave} to $T_{0.1}$ or $T_{0.2}$ show that the ratios of $Q_{p\_\max}$ to Q_{p_um} and of $\Delta T_{plume\_\max}$ to ΔT_{plume_um} are insensitive to different T_{thre_edge}.

[29] For all the cases, Q_{diff_total} is less than 5% and 10% of the $Q_{p\_\max}$, when T_{ave} and $T_{0.2}$ are used as T_{thre_edge}, respectively, indicating that the diffusive heat flux has insignificant effects on plume heat flux reduction as plumes rise.

3.2. The Effects of Adiabatic Cooling and Subadiabatic Temperature on the Plume Heat Flux and Plume Excess Temperature

[30] Our results show a significant depth-dependence of plume heat flux and plume excess temperature. Additionally, plume temperature $T_p(r)$ appears to decrease more rapidly with radius r than the average temperature $T_{ave}(r)$ does, while $T_{ave}(r)$ shows a slight subadiabaticity (e.g., Figure 2a). However, the responsible physical processes were not explored. In this section, we examine the effects of adiabatic cooling and subadiabaticity on the plume excess temperature and plume heat flux.

[31] Let us first present a simple analysis of effects of adiabatic cooling on the plume temperature and plume heat flux. The adiabatic temperature gradient is derived from the condition of isentropy [*Turcotte and Schubert*, 2002]:

$$\frac{dT_{ave}}{dr} = -\frac{\alpha g T_{ave}}{C_p}, \tag{7}$$

Assuming constant α and C_p, this equation can be nondimensionalized by using Earth's radius R_e as the characteristic length scale and the temperature difference between the CMB and surface as the temperature scale. Equation (7) becomes

$$\frac{dT_{ave}}{dr} = -\gamma D_i (T_{ave} + T_s), \tag{8}$$

where D_i is the dissipation number as in equation (2) and $\gamma = R_e/d$ with d as the thickness of the mantle. The solution to this nodimensional equation is

$$T_{ave} + T_s = Ae^{-\gamma D_i r}, \tag{9}$$

where A is a constant.

[32] It can be demonstrated from consideration of the energy balance that the plume temperature T_p also follows an adiabat. We find from our model calculations that the vertical advection and the adiabatic cooling in plume regions are at least one order magnitude larger than the viscous heating and internal heating, because of the large vertical velocity in plume regions (Figures 4a and 4b). The latent heating effects from phase changes are localized in the upper mantle, and two phase changes at 410-km and 670-km depths tend to cancel the latent heating effects of each other.

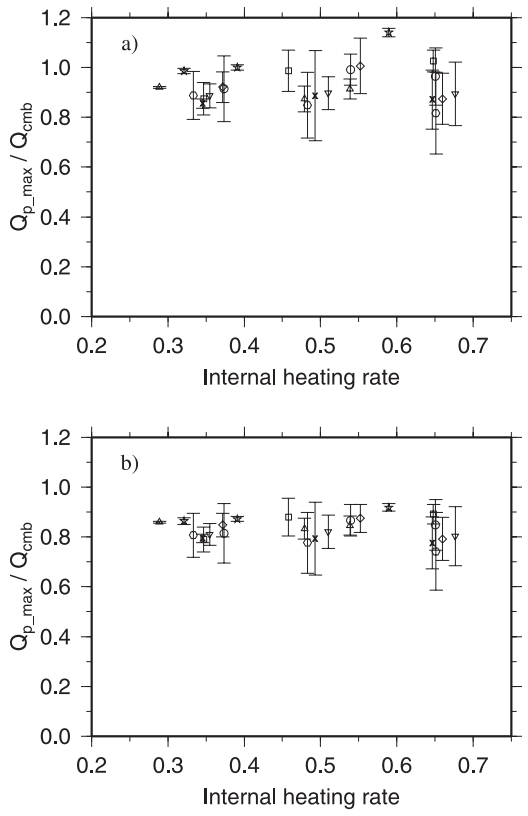

Figure 5. The ratios of the plume heat flux at $r_{\max}$, $Q_{p\_\max}$, to the CMB heat flux, Q_{cmb}, for (a) $T_{thre\_edge} = T_{ave}$, (b) $T_{thre\_edge} = T_{0.2}$. Circles, squares, diamonds, triangles, inverted triangles, stars, hexagon and X represent cases WM01-WM03, WM04-WM06, WM07-WM09, WM10-WM12, WM13-WM15, WM16-WM18, WM19-WM21, and WM22-WM24 respectively. The error bars are for standard deviations over the analyzed time periods.

[33] Let us consider a thin segment of a plume with thickness *dr*. Ignoring the latent heating, viscous heating and internal heating and assuming that plume mass flux is constant at different depth (e.g., Figure 2d), the energy balance for this segment is

$$\rho C_p M\left[(T_p)_t-(T_p)_b\right] = -\rho g M T_p \alpha dr, \tag{10}$$

where ρ, M and T_p are average density, plume mass flux and plume temperature, respectively. $\rho C_p M(T_p)_b$ and $\rho C_p M(T_p)_t$ are therefore advective heat flux flowing in and out of the thin plume segment, respectively. Simplifying this equation leads to

$$\frac{dT_p}{dr} = -\frac{\alpha g T_p}{C_p}. \tag{11}$$

Similarly we nondimensionalize this equation and the solution is

$$T_p + T_s = Be^{-\gamma D_i r}, \tag{12}$$

where B is another constant. Following equations (9) and (12), the plume excess temperature is give by

$$\Delta T_{plume} = T_p - T_{ave} = (B - A)e^{-\gamma D_i r}. \tag{13}$$

The ratio of plume excess temperature at radius r_1 and r_2 is

$$\frac{\Delta T_{plume}(r_1)}{\Delta T_{plume}(r_2)} = e^{\gamma D_i (r_2 - r_1)}. \tag{14}$$

The nondimensional plume heat flux is given by

$$Q_p(r) = M\Delta T_{plume} = M(B - A)e^{-\gamma D_i r}. \tag{15}$$

For constant plume mass flux at different radius (Figure 2d), this implies that the ratio of plume heat flux at radius r_1 and r_2 is

$$\frac{Q(r_1)}{Q(r_2)} = e^{\gamma D_i (r_2 - r_1)}. \tag{16}$$

Equations (14) and (16) show that the ratios of plume

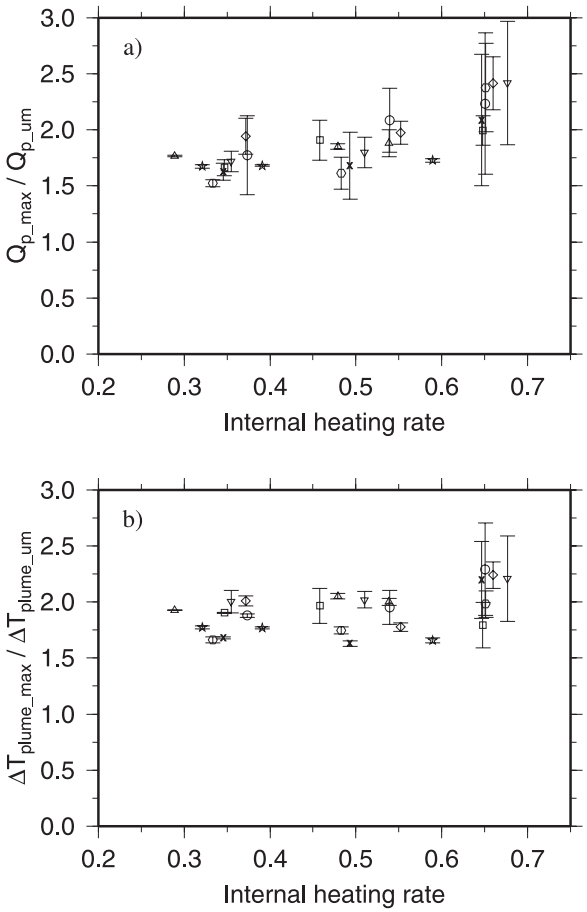

Figure 6. (a) The ratios of plume heat flux at $r_{\max}$, $Q_{p\_\max}$, to plume heat flux at the upper mantle depth (~300 km), Q_{p_um}. (b) The ratios of plume excess temperature at $r_{\max}$, $\Delta T_{plume\_\max}$, to plume excess temperature at the upper mantle depth (~300 km), ΔT_{plume_um}. The symbols are the same as in Figure 5.

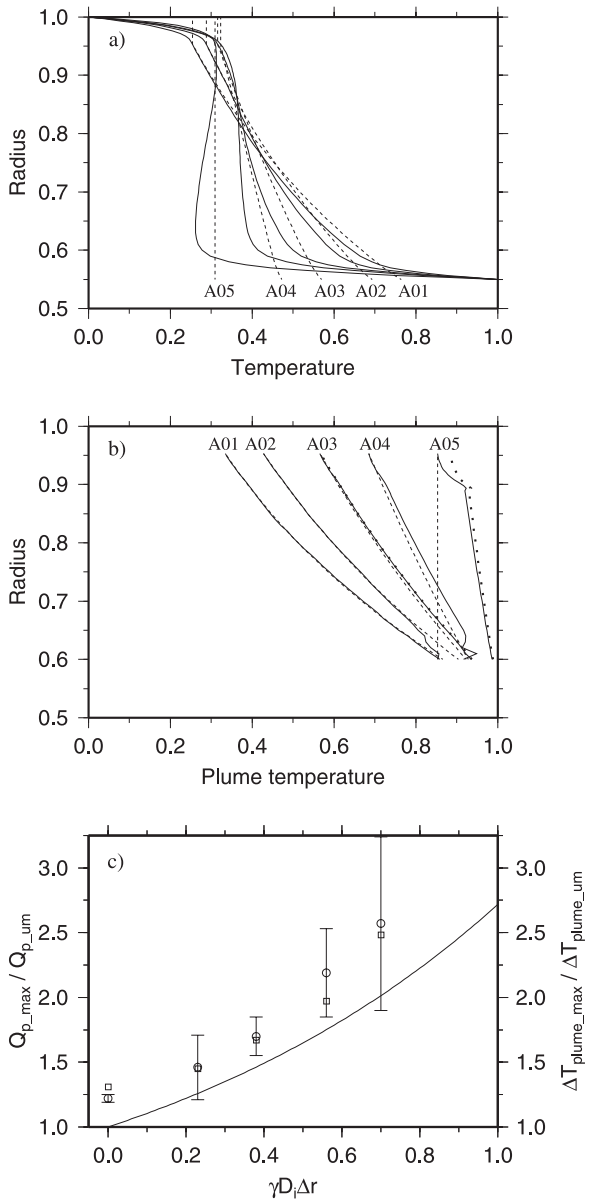

Figure 7. (a) The temperature profiles for cases A01 to A05 (from right to left). The solid and dashed lines represent the average temperature and corresponding adiabatic temperature, respectively. (b) The plume temperature profiles for case A01 to A05 (from left to right). The solid and dashed lines represent the plume temperature and corresponding plume adiabatic temperature, respectively. The thick dotted lines represent the plume temperature for cases A03H and A05H. (c) The ratios of plume heat flux $Q_{p\_\max}$ to Q_{p_um} (circles) and the ratios of plume excess temperature $\Delta T_{plume\_\max}$ to ΔT_{plume_um} (squares) for cases A01 to A05. Notice that the standard deviations for ratios of plume excess temperature are not drawn. The solid line represents the function $e^{\gamma Di \Delta r}$.

excess temperature and plume heat flux at radii r_1 to r_2 are only dependent on the dissipation number D_i and the distance over which plumes rise, $\Delta r = r_2 - r_1$.

[34] For a depth-dependent $\alpha(r)$, the following equation holds,

$$\frac{\Delta T_{plume}(r_1)}{\Delta T_{plume}(r_2)} = \frac{Q(r_1)}{Q(r_2)} = e^{\overline{\alpha}\gamma D_i (r_2 - r_1)}, \tag{17}$$

where $\overline{\alpha}$ is the averaged nondimensional $\alpha(r)$ between r_1 and r_2.

[35] The nearly constant ratios of plume heat flux and plume excess temperature at $r_{\max}$ to those at the upper mantle depth for cases WM01 to WM18 with constant dissipation number $D_i = 1.17$ (Figure 6), are consistent with above analysis. For these cases, $\overline{\alpha}$ and $\Delta r = r_{\max} - r_{um}$ are all similar (Table 3). Therefore it is expected from our analysis that the reduction ratios of plume heat flux and plume excess temperature are similar for these cases. Notice that for cases WM16 to WM18 in nearly stagnant-lid convection, the reduction of plume heat flux and plume excess temperature are smaller than other cases (Figure 6), possibly due to the large $r_{\max}$ (i.e., small Δr) for these three cases (Table 3). Cases WM19 to WM24 have the same $\overline{\alpha}$ and Δr as cases WM01 to WM18, but with smaller dissipation number. Given $\overline{\alpha} = 0.6$ (Table 1) and $\Delta r \sim 0.30$ (Table 3), the ratios of plume heat flux and plume excess temperature at $r_{\max}$ to those at the upper mantle depth should reduce by 13% and 17% for $D_i = 0.82$ and $D_i = 0.70$, respectively, which is consistent with our results (Figure 6). The agreement between the theory and the modeling results suggests that the steeper adiabatic gradient of plumes compared with the ambient mantle are the main cause for the reduction of plume heat flux and plume excess temperature as plumes rise. The steeper adiabatic gradient for plumes results from higher plume temperature which causes a larger magnitude of adiabatic heating term for plumes.

[36] To further test this theory, we compute five simplified cases (cases A01 to A05 in Table 2) in which the two phase changes are removed and thermal diffusivity κ and coefficient of thermal expansion α are uniform throughout the mantle. For these five cases, κ is 1.59×10^{-6} m^2/s, which is the averaged value of the mantle for earlier cases. However, α or dissipation number D_i is variable in these five cases (Table 2). Rayleigh number Ra is also varied according to the variation in α, except for case A05 with $D_i = 0$, for which Ra is taken as the averaged value of other four cases.

[37] For case A01 with the largest $D_i = 1.05$, while the average temperature $T_{ave}(r)$ shows slight subadiabaticity (Figure 7a), the plume temperature $T_p(r)$ follows the plume adiabat very well (i.e., equation (12) and Figure 7b). $T_{ave}(r)$ for all these five cases display slight subadiabaticity, but $T_p(r)$ follows the adiabat quite well (Figures 7a and 7b). Note that near the CMB, there are some fluctuations in $T_p(r)$ and this is caused by the variations of the number of plumes detected with our algorithm near the CMB. This is expected as plumes near the CMB are not as well defined. Although thermal convection has reached a statistically steady state, plumes are still continuously generated and merge near the CMB, thus causing the number of plumes to vary with time. Since $T_p(r)$ is the average value over all the plumes, it is sensitive to the number of plumes, particularly near the CMB.

[38] The ratios of $\Delta T_{plume\_\max}$ to ΔT_{plume_um} and the ratios of $Q_{p\_\max}$ to Q_{p_um} for these five cases follow the

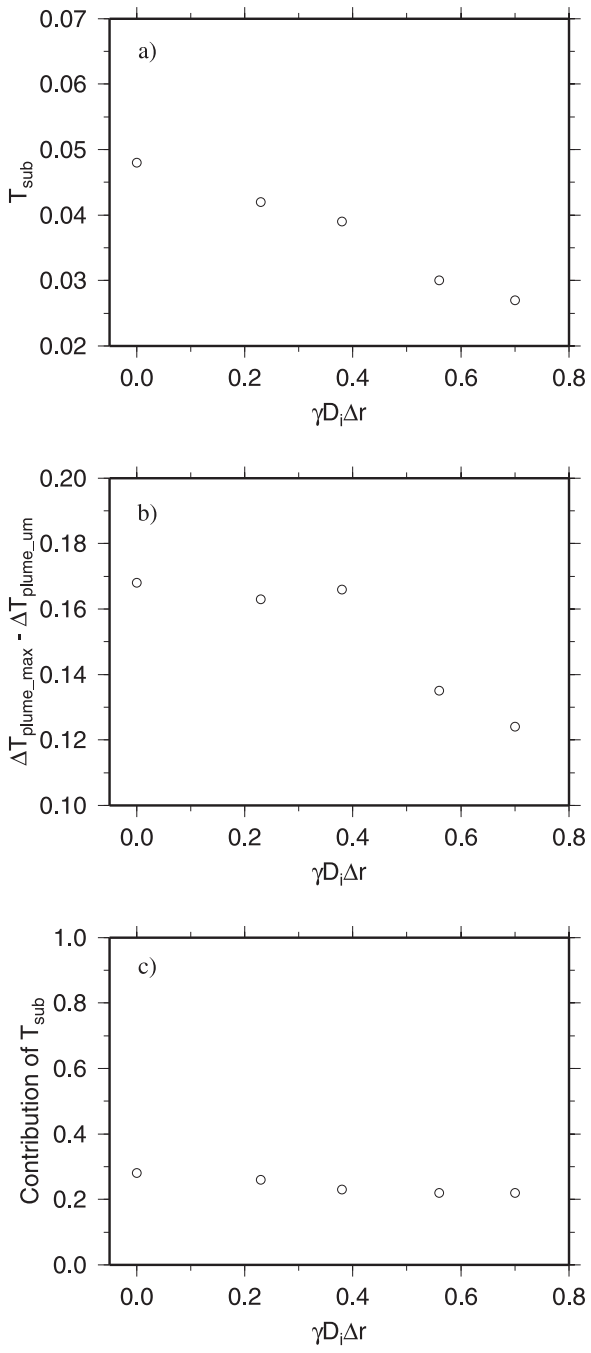

Figure 8. The subadiabatic temperatures and their contributions to the reduction of plume heat flux for case A01 to A05. (a) The subadiabatic temperatures. (b) The reduction of plume excess temperature from $r_{\max}$ to r_{um}. (c) The contribution of subadiabatic temperature to the reduction of plume heat flux.

trend as predicted by equations (14) and (16) (i.e., $e^{\gamma Di \Delta r}$) reasonably well, but the numerical models uniformly overpredict the ratios relative to the theory (Figure 7c), which we attribute to the effects of subadiabaticity. Subadiabatic temperatures for cases A01 to A05 are determined by measuring the differences between $T_{ave}(r)$ and $T_{adi}(r)$ at $r_{\max}$ (Figure 8a). Subadiabatic temperature decreases in general with dissipation number. The total reduction in ΔT_{plume} from $r_{\max}$ to r_{um} is also found to generally decrease with D_i (Figure 8b). The effect of the subadiabatic temperature on the reduction of plume excess temperature and plume heat flux can be determined by computing the ratio of subadiabatic temperature to the total reduction of ΔT_{plume} from $r_{\max}$ to r_{um}. For all the five cases, these ratios range from 20% to 30% (Figure 8c). This suggests that the subadiabatic temperature plays a secondary role in reducing the plume excess temperature and plume heat flux, compared with adiabatic cooling.

[39] In case A05 with $D_i = 0$, there is no adiabatic cooling, but the plume temperature still decreases gently in the lower mantle but more rapidly in the upper mantle (Figures 7a and 7b). We attribute this to the resolution problem and also possibly relatively large thermal diffusion. In case A05, the average interior temperature is nearly constant at 0.3. However, the plume temperature is close to 1.0. The viscosity contrast between plumes and the ambient mantle is thus on the order of 10^2, while for other cases, e.g., case A03, the viscosity contrast is just about 20. The large viscosity and temperature contrasts may require more resolution in resolving the plumes [*Leitch et al.*, 1996; *Lin and van Keken*, 2005]. In the upper mantle, since the viscosity is reduced by a factor of 30, this resolution problem may become even more serious. After we increase the resolution for case A05 by a factor of 2 (case A05H), the results are improved to some extent (Figure 7b). However, increasing resolution for case A03 (case A03H) with moderate D_i does not affect the plume temperature at all (Figure 7b), suggesting that the resolution for other cases is adequate.

[40] We now return to those more realistic cases (WM01 to WM24) with the phase changes and depth-dependent thermodynamic parameters. For these cases, the ratios of plume heat flux above the CMB at $r_{\max}$, $Q_{p\_\max}$, to plume heat flux at the upper mantle depth, Q_{p_um}, and the ratios of the corresponding plume excess temperatures are all close to be 2.0 (Figure 6). As indicated earlier, the reduction in plume heat flux and plume excess temperature as plume rise is controlled mainly by the steeper adiabatic gradient of plumes compared with the ambient mantle. However, subadiabatic temperature also contributes to this reduction. We determined the subadiabatic temperatures for these cases as we did for those simplified cases (cases A01 to A05). The subadiabatic temperatures for these cases are generally between 0.01 and 0.07 (Figure 9a). Supposing that the total temperature difference between CMB and surface is ~3400 K [*Boehler et al.*, 1995], the subadiabatic temperature ranges between 35 K and 240 K. Notice that for large internal heating rate (>50%), the subadiabatic temperatures are generally between 0.01 and 0.05, or 35 K and 170 K (Figure 9a). The contribution of subadiabatic temperature to the reduction of plume heat flux and plume excess temperature, determined in the same way as for cases A01 to A05, is similar, ranging from 20% to 30% for cases WM01 to WM24 (Figure 9b). This suggests that subadiabatic temperature plays only a secondary role in causing the reduction in plume heat flux and plume excess temperature as plumes rise.

3.3. Constraints on the Internal Heating of the Mantle From Plume Heat Flux, Plume Excess Temperature, and Upper Mantle Temperature

[41] Various observations suggest that the plume excess temperature and plume heat flux in the upper mantle are

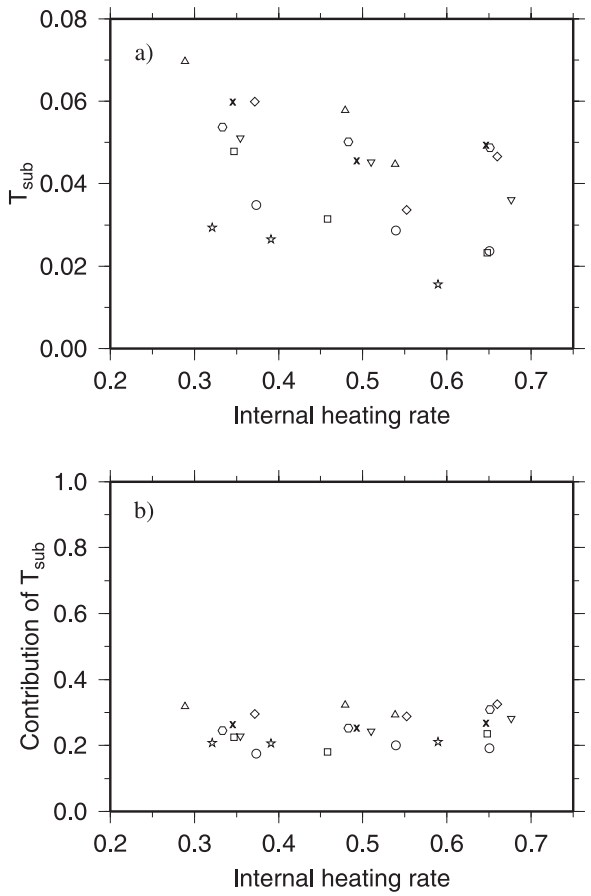

Figure 9. (a) The subadiabatic temperatures for cases WM01 to WM24 versus internal heating rates. (b) The contribution of subadiabatic temperature to the reduction of plume heat flux, for cases WM01 to WM24 versus internal heating rates. The symbols are the same as in Figure 5.

250–350 K and 2.4–3.6 TW, respectively [*Schilling*, 1991; *Farnetani*, 1997; *Davies*, 1988; *Sleep*, 1990], and that the upper mantle averaged temperature T_{um} is ~1280°C [*Turcotte and Schubert*, 2002]. This implies that at the upper mantle depth the plume excess temperature normalized by the ambient mantle temperature and plume heat flux normalized by surface heat flux are 19%–27% and 6%–10%, respectively. The upper mantle temperature normalized by the temperature difference across the mantle is 0.338–0.455, where the temperature difference across the mantle is taken as 3400 ± 500 K with relatively large uncertainties [*Boehler et al.*, 1995]. *Zhong* [2006] quantified these observables in his models and suggested that mantle internal heating rate in whole mantle convection models is required to be ~65% in order to reproduce these observations.

[42] We also quantified the plume heat flux, plume excess temperature and averaged mantle temperature at 300 km depth for cases WM01 to WM15 and WM19 to WM24, and compared them with those inferred from observations. We excluded cases WM16 to WM18 because they do not have a mobile lid. We use the background temperature in the upper mantle, T_{bg}, instead of the average temperature T_{ave} to define the plume excess temperature and plume heat flux, where T_{bg} is the average temperature excluding cold downwellings [*Zhong*, 2006]. Given that the plume heat flux is measured from the bathymetry surrounding a proposed plume, it is more appropriate to use T_{bg} as the average temperature instead of T_{ave}. However, the difference between T_{ave} and T_{bg} is usually very small in upper mantle, 1%, from our models. Compared with *Zhong* [2006], the current study covers a larger model parameter space including higher activation energy, variable lithospheric viscosity and variable dissipation number and has a higher resolution.

[43] Our results show that the normalized plume heat flux and plume excess temperature decrease with the internal heating rate, but the background temperature at the upper mantle depth, T_{um}, increases with the internal heating rate (Figures 10a to 10d). Increasing T_{thre_edge} in the plume detection scheme from $T_{thre\_edge} = T_{bg}$ to $T_{thre\_edge} = T_{bg} + 0.2(T_{\max} - T_{bg})$ only slightly decreases the plume heat flux in the upper mantle (Figures 10a and 10b).

[44] The plume temperature in the upper mantle, T_{p_um}, is about 0.52 for cases WM01 to WM15 with dissipation number D_i = 1.17, but it is ~0.64 for cases WM19 to WM24 with D_i between 0.70 and 0.82. From equation (12) and for a depth-dependent $\alpha(r)$, the plume temperatures in the upper mantle $(T_{p\_um})_1$ for cases with dissipation number $(D_i)_1$ and $(T_{p\_um})_2$ for cases with $(D_i)_2$ can be related as following:

$$\frac{(T_{p\_um})_1 + T_s}{(T_{p\_um})_2 + T_s} = e^{\overline{\alpha}\gamma\left((D_i)_2 - (D_i)_1\right)\Delta r}, \tag{18}$$

where the normalized surface temperature T_s is ~0.07 for a range of CMB temperature. For cases WM19 to WM24, given $\overline{\alpha}$ = 0.6 (Table 1) and $\Delta r \sim 0.30$ (Table 3), the plume temperature in the upper mantle should increase by 17% and 24% for D_i = 0.82 and D_i = 0.70, respectively, compared to that for cases WM01 to WM15, which are consistent with our numerical results (Figure 10e). Notice that when the dissipation number is decreased, the background temperature increases (Figure 10d). The both increased plume temperature and background temperature do not affect significantly the distribution of plume heat flux and plume excess temperature versus internal heating rate, especially at relatively large internal heating rate (Figures 10a and 10c).

[45] To reproduce all the plume-related observations, the internal heating rate of mantle convection is required to be ~70%. This is consistent with *Zhong* [2006] although the required internal heating rate in the current study is a little higher than that obtained by *Zhong* [2006], possibly as a result of our improved resolution.

4. Discussion and Conclusion

[46] We have quantified heat transfer of upwelling plumes in 3-D regional spherical models of mantle convection. Our models employ temperature- and depth-dependent viscosity, depth-dependent coefficient of thermal expansion and thermal diffusivity, and extended Boussinesq approximation. Our models use different Rayleigh number, internal heating rate, activation energy, lithospheric viscosities and dissipation number. The primary results from our calculations can be summarized as following.

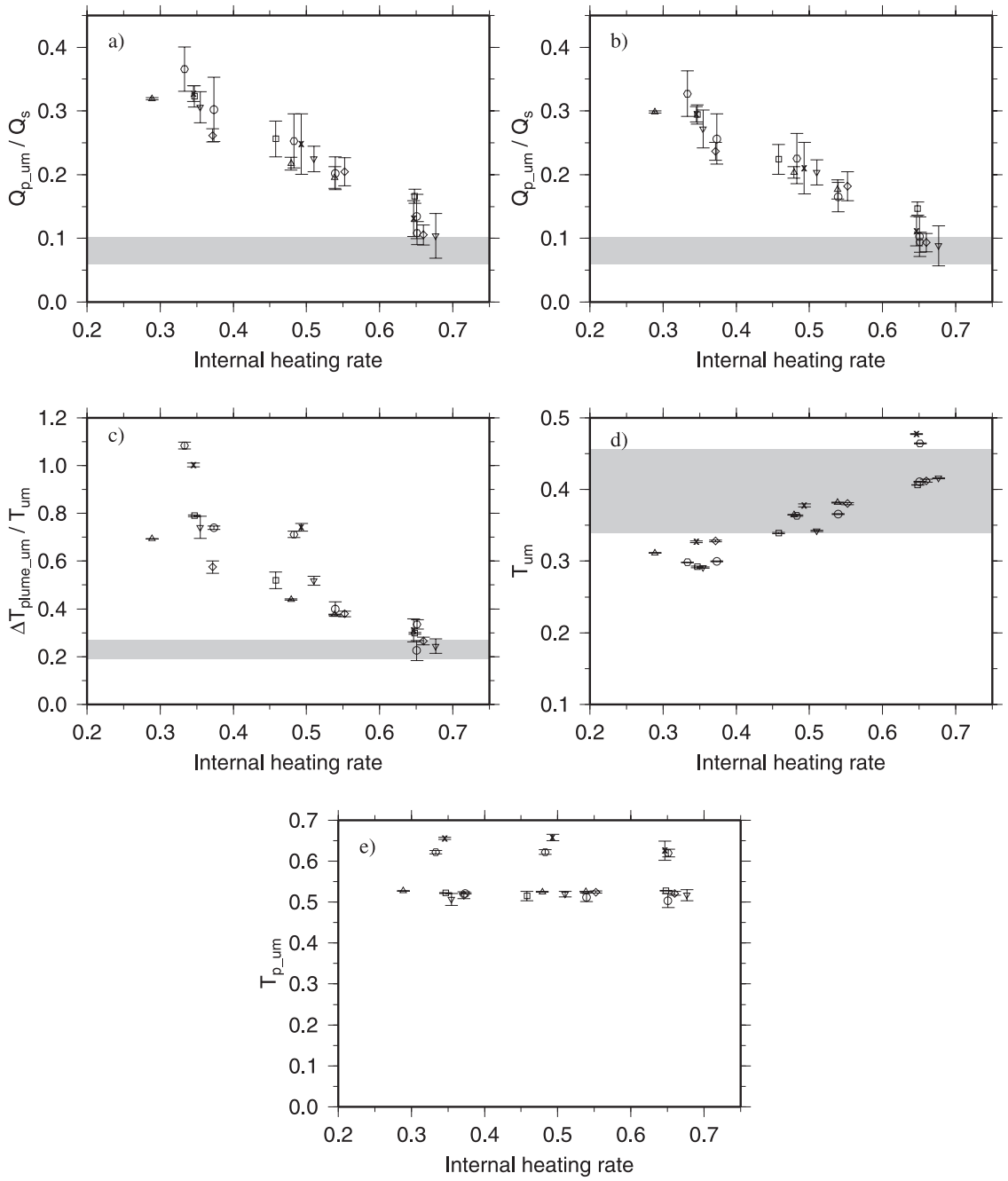

Figure 10. (a) The ratios of the plume heat flux in the upper mantle (~300 km depth), Q_{p_um}, to the surface heat flux Q_s, using T_{bg} as T_{thre_edge}. (b) The same as Figure 10a, except using $T_{bg} + 0.2(T_{\max} - T_{bg})$ as T_{thre_edge}. (c) The ratios of the plume excess temperature in the upper mantle ΔT_{plume_um} to the background temperature in the upper mantle T_{um}. (d) The background temperature in the upper mantle, T_{um}. (e) The plume temperature in the upper mantle, T_{p_um}. The symbols are the same as in Figure 5. The shaded zones represent the ranges of observations.

[47] (1) Nearly 80%–90% of the CMB heat flux is carried by upwelling plumes immediately above the thermal boundary layer of the CMB. However, the plume heat flux decreases by approximately a factor of two as plumes rise from near the CMB to the upper mantle for models considered in this study. The plume excess temperature also decreases by a similar factor as plumes rise.

[48] (2) This reduction in plume heat flux and plume excess temperature is controlled mainly by the steeper adiabatic gradient of plumes due to their elevated temperature. Adiabatic cooling of plumes causes the plume heat flux and plume excess temperature to decrease by a factor of $e^{\overline{\alpha\gamma_D i}\Delta r}$ for plumes to ascend over a distance Δr. Adiabatic cooling of plumes contributes 70%–80% to the plume heat flux reduction from above the CMB to the upper mantle.

[49] (3) Subadiabatic temperature contributes 20%–30% to the plume heat flux reduction and its effect is secondary to the adiabatic cooling. For CMB temperature of 3400°C, the subadiabatic temperature from our models ranges from 35 K to 170 K for >50% internal heating rate.

[50] (4) This study covering larger parameter space with higher resolution confirms that the mantle internal heating rate is required to be ~70% to reproduce the observations of plume heat flux, plume excess temperature and upper mantle temperature, as reported by *Zhong* [2006].

[51] An important implication of our results is about to what extent the plume heat flux estimated from the plate motion and swell topography by *Davies* [1988] and *Sleep* [1990] represents the core heat flux. *Davies* [1988] and *Sleep* [1990] considered their estimated plume heat flux for the upper mantle to be the same as the core heat flux. Our results suggest that while the core heat flux is largely (80%-90%) released through plumes above the CMB, supporting the original suggestion by *Davies* [1988] and *Sleep* [1990], the plume heat flux also decreases by a factor of two or more as plumes rise from near the CMB to the upper mantle. Therefore the estimated plume heat flux for the upper mantle by *Davies* [1988] and *Sleep* [1990] significantly underestimates the CMB heat flux by at least a factor of 2.

[52] That the CMB heat flux was significantly underestimated by the estimated plume heat flux from swell topography was also suggested by *Labrosse* [2002], *Bunge* [2005], *Mittelstaedt and Tackley* [2006] and *Sleep* [2006], but for different reasons as reviewed in the introduction section. *Labrosse* [2002] and *Mittelstaedt and Tackley* [2006] quantified plume heat flux in their models. They found that plume heat flux represents much smaller fraction of the CMB heat flux, but did not observe significant plume heat flux reduction as plumes rise. The difference between their results and ours may be caused by model geometry and model assumptions. Our models are formulated in 3-D spherical geometry with adiabatic heating and more realistic rheology, while Laborosse's models are in 3-D Cartesian geometry with constant viscosity and without adiabatic heating (i.e., Boussinesq approximation). *Mittelstaedt and Tackley* [2006] considered various 2-D models with realistic rheology, but they did not consider 3-D spherical geometry and adiabatic heating either. Models with a 3-D spherical geometry tend to give a smaller mantle average temperature, thus enhancing the plume heat flux, compared with Cartesian models or 2-D cylindrical models. Adiabatic cooling of plumes due to plumes' large temperature is important in reducing the plume excess temperature and plume heat flux as plumes rise, as suggested by *Zhong* [2006], and clearly demonstrated in the current study.

[53] *Bunge* [2005] suggested that the plume heat flux may decrease by a factor of 3 as plumes rise from the CMB to the upper mantle. However, he emphasized the role of subadiabatic temperature that may be as large as 500 K from his models. We also observe subadiabatic temperatures for all of our cases, but with much smaller amplitude (mostly less than 200 K). Our calculations show that the subadiabatic temperature may contribute up to 30% to the reduction of plume heat flux in our models.

[54] Our study indicates that the internal heating rate for whole mantle convection needs to be ~70%. This suggests that the CMB heat flux is ~11 TW, taking convective surface heat flux for the present-day mantle as 36 TW. This CMB heat flux is more than three times of what was suggested by *Davies* [1988] and *Sleep* [1990], but is consistent with recent estimates from seismic studies [*van der Hilst et al.*, 2007; *Hernlund et al.*, 2005; *Lay et al.*, 2006]. It should be pointed out that the plume heat flux reduction ratio increases slightly with the internal heating rate and the ratio is ~2.5 for internal heating rate of ~70% (Figure 6).

[55] Furthermore, our study suggests a simple relation of the plume temperature in the upper mantle to the CMB temperature and the averaged coefficient of thermal expansion for the mantle α. As shown in Figure 10e, the nondimensional plume temperatures in the upper mantle are nearly 0.52 for cases WM01 to WM15 in which the average coefficient of thermal expansion is 2.4×10^{-5}/K. Given that the ambient temperature and the plume excess temperature in the upper mantle are 1280°C [*Turcotte and Schubert*, 2002] and 250–350°C [*Schilling*, 1991; *Farnetani*, 1997] respectively, the plume temperature in the upper mantle (~300 km depth) is 1530–1630°C. This suggests that the CMB temperature is 2940–3130°C, or 3220–3410 K, which is on the low end compared with previous studies, but remains in the range of uncertainties [*Boehler et al.*, 1995]. If the recent estimate of CMB temperature of 3950 K based on a seismic study is valid [*van der Hilst et al.*, 2007], then this suggests that the coefficient of thermal expansion for the mantle is larger than that used in our studies. Supposing that the CMB temperature is 3950 K [*van der Hilst et al.*, 2007], the nondimensional plume temperature in the upper mantle is 0.42–0.44, which suggests the average coefficient of thermal expansion for the mantle is approximately 3.2×10^{-5}/K.

[56] The physical processes in CMB regions are important but also complicated. In this study, we focus on plume dynamics and its implications for the CMB temperature and heat flux. A number of related areas deserve more studies. Subadiabatic temperature from mantle convection studies are rather different [*Bunge*, 2005; *Bunge et al.*, 2001; *Zhong*, 2006], and more studies are needed to understand the difference, given its relevance to mantle dynamics and seismic properties of the mantle. Our models are computed in the whole mantle convection regime, while global seismic tomography and waveform studies indicate that the mantle is probably chemically heterogeneous [*Masters et al.*, 2000; *Ni et al.*, 2002; *Wen et al.*, 2001]. The results from current study therefore should be examined in thermochemical convection models as in the work of *Zhong* [2006]. Recent studies suggested that there may be a peroviskite to post-peroviskite phase change near the CMB [*Murakami et al.*, 2004]. It is necessary for the future work to integrate this phase change into the numerical models and investigate its effects on the dynamics of plumes [*Nakagawa and Tackley*, 2006; *Kameyama and Yuen*, 2006]. The extended-Boussinesq approximation used in our models is a good approximation to simulate the adiabatic effect in the mantle, but future studies on plume dynamics may need to employ fully compressible convection models [*Tan and Gurnis*, 2005; *Ita and King*, 1998]. Finally, our models are for quasi-steady state thermal convection while the Earth cools over time. It is also interesting to include secular cooling of

the mantle in our models and study its effects on the conclusions.

[57] **Acknowledgments.** Reviews by Geoff Davies and Norm H. Sleep helped to improve this manuscript. This research was supported by National Science Foundation and David and Lucile Packard Foundation.

References

Bercovici, D., G. Schubert, and G. A. Glatzmaier (1992), Three-dimensional convection of an infinite-Prandtl number compressible fluid in a basally heated spherical shell, *J. Fluid Mech.*, *239*, 683–719.

Boehler, R., A. Chopelas, and A. Zerr (1995), Temperature and chemistry of the core-mantle boundary, *Chem. Geol.*, *120*, 199–205.

Bunge, H. (2005), Low plume excess temperature and high core heat flux inferred from non-adiabatic geotherms in internally heated mantle circulation models, *Phys. Earth Planet. Inter.*, *153*, 3–10.

Bunge, H. P., Y. Ricard, and J. Matas (2001), Non-adiabaticity in mantle convection, *Geophys. Res. Lett.*, *28*, 879–882.

Christensen, U. R., and D. A. Yuen (1985), Layered convection induced by phase transitions, *J. Geophys. Res.*, *90*, 10,291–10,300.

Davies, G. F. (1988), Ocean bathymetry and mantle convection: 1. Large-scale flow and hotspots, *J. Geophys. Res.*, *93*, 10,467–10,480.

Davies, G. (Ed.) (1999), *Dynamic Earth: Plates, Plumes and Mantle Convection*, 458 pp., Cambridge Univ. Press, New York.

Farnetani, C. (1997), Excess temperature of mantle plumes: The role of chemical stratification across D″, *Geophys. Res. Lett.*, *24*, 1583–1586.

Hernlund, J., C. Thomas, and P. J. Tackley (2005), A doubling of the post-perovskite phase boundary and structure of the earth's lowermost mantle, *Nature*, *434*, 882–886.

Hewitt, J. M., D. P. Mackenzie, and N. O. Weiss (1975), Dissipative heating in convective flows, *J. Fluid Mech.*, *68*, 721–738.

Ita, J. J., and S. D. King (1998), The influence of thermodynamic formulation on simulations of subduction zone geometry and history, *Geophys. Res. Lett.*, *125*, 1463–1466.

Jarvis, G. T., and D. P. McKenzie (1980), Convection in a compressible fluid with infinite Prandtl number, *J. Fluid Mech.*, *96*, 515–583.

Kameyama, M., and D. A. Yuen (2006), 3-D convection studies on the thermal state in the lower mantle with post-perovskite transition, *Geophys. Res. Lett.*, *33*, L12S10, doi:10.1029/2006GL025744.

Labrosse, S. (2002), Hotspots, mantle plumes and core heat loss, *Earth Planet. Sci. Lett.*, *199*, 147–156.

Lay, T., J. Hernlund, E. J. Garnero, and M. S. Thorne (2006), A post-perovskite lens and D″ heat flux beneath the central pacific, *Science*, *314*, 1272–1276.

Leitch, A., V. Steinbach, and D. A. Yuen (1996), Centerline temperature of mantle plumes in various geometries: Incompressible flow, *J. Geophys. Res.*, *101*, 21,829–21,846.

Lin, S.-C., and P. van Keken (2005), Multiple volcanic episodes of flood basalts caused by thermochemical plumes, *Nature*, *436*, 250–252.

Masters, G., G. Laske, H. Bolton, and A. Dziewonski (2000), The relative behavior of shear velocity, bulk sound speed, and compressional velocity in the mantle: Implications for chemical and thermal structure, in *Earth's Deep Interior: Mineral Physics and Tomography from the Atomic to the Global Scale*, *Geophys. Monogr. Ser.*, edited by S. Karato, et al., pp. 63–87, AGU, Washington, D.C.

Mittelstaedt, E., and P. J. Tackley (2006), Plume heat flux is much lower than CMB heat flow, *Earth Planet. Sci. Lett.*, *241*, 202–210.

Moresi, L., and M. Gurnis (1996), Constraints on the lateral strength of slabs from three-dimensional dynamic flow models, *Earth Planet. Sci. Lett.*, *138*, 15–28.

Morgan, W. (1971), Convection plumes in the lower mantle, *Nature*, *230*, 42–43.

Murakami, M., K. Hirose, K. Kawamura, N. Sata, and Y. Ohishi (2004), Post-perovskite phase transition in $M_gS_iO_3$, *Science*, *304*, 855–858.

Nakagawa, T., and P. J. Tackley (2006), Three-dimensional structures and dynamics in the deep mantle: Effects of post-perovskite phase change and deep mantle layering, *Geophys. Res. Lett.*, *33*, L12S11, doi:10.1029/2006GL025719.

Ni, S., E. Tan, M. Gurnis, and D. Helmberger (2002), Sharp sides to the African superplume, *Science*, *296*, 1850–1852.

Schilling, J. G. (1991), Fluxes and excess temperatures of mantle plumes inferred from their interaction with migrating midocean ridges, *Nature*, *352*, 397–403.

Sleep, N. H. (1990), Hotspots and mantle plumes: Some phenomenology, *J. Geophys. Res.*, *95*, 6715–6736.

Sleep, N. H. (1992), Time dependence of mantle plumes: Some simple theory, *J. Geophys. Res.*, *97*, 20,007–20,019.

Sleep, N. H. (2006), Mantle plumes from top to bottom, *Earth Sci. Rev.*, *77*, 231–271.

Tan, E., and M. Gurnis (2005), Metastable superplumes and mantle compressibility, *Geophys. Res. Lett.*, *32*, L20307, doi:10.1029/2005GL024190.

Turcotte, D. L., and G. Schubert (Eds.) (2002), *Geodynamics*, 2nd ed., 456 pp., Cambridge Univ. Press, New York.

Turcotte, D. L., A. T. Hsui, K. E. Torrance, and G. Schubert (1974), Influence of viscous dissipation on Benard convection, *J. Fluid Mech.*, *64*, 369–374.

van der Hilst, R. D., M. V. de Hoop, P. Wang, S.-H. Shim, P. Ma, and L. Tenorio (2007), Seismostratigraphy and thermal structure of earth's core-mantle boundary region, *Science*, *315*, 1813–1817.

Wen, L., P. Silver, D. James, and R. Kuehnel (2001), Seismic evidence for a thermo-chemical boundary layer at the base of the earth's mantle, *Earth Planet. Sci. Lett.*, *189*, 141–153.

Zhang, S., and D. A. Yuen (1996), Various influences on plumes and dynamics in time-dependent, compressible mantle convection in 3-d spherical shell, *Phys. Earth Planet. Inter.*, *94*, 241–267.

Zhong, S. (2006), Constraints on thermochemical convection of the mantle from plume heat flux, plume excess temperature, and upper mantle temperature, *J. Geophys. Res.*, *111*, B04409, doi:10.1029/2005JB003972.

W. Leng and S. Zhong, Department of Physics, University of Colorado, Boulder, CO 80309, USA. (wei.leng@colorado.edu)